This article has been accepted for inclusion in a future issue of this journal. Content is final as presented, with the exception of pagination.

Piezoresistive Sensors Array for Multijoint Motion Estimation Application

Zinan Cen, *Member, IEEE*, Fraser Robinson, *Member, IEEE*, Goldie Nejat, *Member, IEEE*, and Hani E. Naguib

***Abstract*—With the emergence of digital healthcare, comes the need for an unobtrusive method for long-term motion monitoring. In recent years, wearable sensors have been utilized for motion monitoring to replace the conventional camera-based systems. Despite several attempts at measuring joint angles, designs for affordable and low power-consuming systems were lacking. This article explored the usage of ten low-cost, energy-efficient conductive polymer composite-based strain sensors composed of thermoplastic polyurethane elastomer matrix and multiwalled carbon nanotube (CNT) to create a smart clothing system for the measurement of elbow and shoulder joint angles. To overcome the time-varying and nonlinear behavior of the proposed strain sensor, a novel architecture of a convolutional neural network was designed to enhance the mapping of sensor signals to joint angles by extracting inter-sensor spatial and temporal information. Strain sensors with different concentrations were fabricated and characterized. It was found that 4 wt% CNT produced the highest sensitivity due to the highest degree of macrostructural damage. Motion monitoring performance was evaluated on one volunteer performing different actions and overall normalized root mean squared errors for elbow angle and shoulder Euler angles were 6.77%, 7.19%, 6.31%, and 8.22%, respectively.**

***Index Terms*—Joints, motion estimation, piezoresistive devices, sensor arrays, smart textiles, strain sensors, wearable sensors.**

Manuscript received 21 September 2023; revised 8 January 2024; accepted 15 February 2024. Recommended by Technical Editor S. Kukreja and Senior Editor Y. Li. This work was supported in part by AGE-WELL Inc., in part by the Natural Sciences and Engineering Research Council of Canada (NSERC) discovery grants, and in part by the Canada Research Chairs (CRC) Program. *(Corresponding author: Hani E. Naguib.)*

Zinan Cen is with the Autonomous Systems and Biomechatronics Laboratory of the University of Toronto, Toronto, ON M5S3G8, Canada, and also with the Toronto Smart Materials and Structures TSMART Laboratory of the University of Toronto, Toronto, ON M5S3G8, Canada (e-mail: zinan.cen@mail.utoronto.ca).

Fraser Robinson and Goldie Nejat are with the Autonomous Systems and Biomechatronics Laboratory of the University of Toronto, Toronto, ON M5S3G8, Canada (e-mail: fraser.robinson@mail.utoronto.ca; nejat@mie.utoronto.ca).

Hani E. Naguib is with the Toronto Smart Materials and Structures TSMART Laboratory of the University of Toronto, Toronto, ON M5S3G8, Canada (e-mail: naguib@mie.utoronto.ca).

Color versions of one or more figures in this article are available at https://doi.org/10.1109/TMECH.2024.3371875.

Digital Object Identifier 10.1109/TMECH.2024.3371875

I. Introduction

As DIGITAL healthcare emerges, motion-capturing technology has gained increasing importance since it can provide an unobtrusive method of capturing motion data on patients with mobility impairments, which can be used to increase efficiency in assessment tasks. For example, a full body suit with 60 reflective markers and 16 cameras was used for tracking the posture of the patients, and features such as posture stability and action tremor were computed and used to classify symptom severity of Parkinson's disease patients [1]. A two-camera marker-less system was used in [2] for skeletal tracking of patients. Shoulder-elbow-wrist and head-hand distance were extracted and used to predict Fugl-Meyer assessment scores in a poststroke physical rehabilitation setting.

In recent years, there has been a growing interest in the development of "smart clothing" by integrating sensors into daily garments for motion-tracking applications. In general, smart clothing aims to overcome the limitations of camera-based motion monitoring systems, such as occlusion, portability, strict workspace requirements, and privacy concerns. Despite numerous attempts at accurately measuring joint angles, there is a lack of practical solutions for long-term motion estimation.

Inertial sensors are the most attempted modality for motion tracking in smart clothing. System-on-chip (SoC) is often created using multiple inertial sensors including a tri-axial accelerometer and a tri-axial gyroscope, as well as an additional tri-axial magnetic sensor to compensate signal drift. Such SoC, commonly referred to as inertial measurement unit (IMU) uses extended Kalman filters-based algorithms to fuse its signals to estimate the orientation of the body segment the IMU is attached to relative to the geomagnetic field [3]. To track joint motions, two IMUs are placed on either side of the joint. Relative changes between the estimated orientation frames of the IMUs are then used to extract the joint angles. Joint angle extraction can be achieved through a rotation matrix estimation based algorithm [4], complimentary filter based algorithm [5], and probabilistic graphical models [6]. However, these methods rely on information from magnetometers, which suffer significantly from magnetic disturbances in indoor environments [7]. In addition, IMUs have high power consumption, limiting their long-term monitoring capability [8].

An alternative modality to inertial sensors is strain sensors, which produce signals proportional to subjected to strain. In contrast to IMUs, these stretchable strain sensors can be

1083-4435 © 2024 IEEE. Personal use is permitted, but republication/redistribution requires IEEE permission.
See https://www.ieee.org/publications/rights/index.html for more information.

Authorized licensed use limited to: The University of Toronto. Downloaded on June 08,2024 at 19:06:41 UTC from IEEE Xplore. Restrictions apply.

This article has been accepted for inclusion in a future issue of this journal. Content is final as presented, with the exception of pagination.

attached directly to the joints. For 1 degree of freedom (DOF) motions such as knee bending and leg motion in the sagittal plane, a simple linear model can be constructed to map sensor signal to joint bending angle [9], [10]. However, for multi-DOF joints such as shoulder joint, hip joint, and ankle joint, it is challenging to obtain one-to-one mapping between one sensor and one desired joint angle, as the strain signal results from the combination of all joint angles. As a result, an array of sensors is often placed around the joint to vary the insight from the joint angles. To address the complexity of the sensor signal-joint angle relationship, machine learning algorithms were often used as the mapping model. For example, fully connected neural network was utilized to map signals from a 4-sensor array to a 3-DOF ankle joint angle [11], convolutional neural network (CNN) was used to map 9-sensor array to the combination of 3-DOF hip, 1-DOF knee, and 2-DOF ankle joint angles [12], and CatBoost regression model was used to map 8-sensor array to 3-DOF shoulder joint angles [13]. Although mapping models in existing studies often included sensor signals across various timesteps to extract temporal information, intra-array spatial information, such as relative sensor locations, was often overlooked. The 2-D convolutional kernels in the CNN model extract information from neighboring signals in the 2-D input matrix. This mechanism can be exploited by encoding both intersensor spatial and temporal information in the input matrix to facilitate simultaneous feature extraction in both dimensions. The usage of CNN in [12] took advantage of encoding temporal information. However, the arrangement of sensor order in the input was arbitrary and can enhance spatial information by enforcing the desired arrangement order.

Various strain sensors have been used in these motion-tracking applications. They can generally be classified into two types based on their output signals: capacitive sensors that generate capacitance signals and resistive sensors that produce resistance signals. Capacitive strain sensors typically consist of a three-layer structure, featuring a stretchable dielectric layer sandwiched between two stretchable electrode layers. Silicon, polyurethane (PU), and Ecoflex are commonly used as the dielectric layer [10], [14], whereas carbon nanotubes (CNTs) and conductive knit fabric have been used as electrodes [14], [15]. Capacitive sensors commonly exhibit high linearity, low hysteresis, but low sensitivity [15], while resistive sensors typically have high sensitivity but low linearity. However, the nonlinearity and time-varying behavior of resistive sensors can be addressed through computational means such as long short-term memory neural network [16]. Conductive sensors require a relatively large sensing area to achieve sufficient baseline capacitance values to combat parasitic capacitance in the readout circuit [15]. In contrast, resistive sensors achieve small footprint, allowing for a dense array over small area [17]. Moreover, resistive sensors are advantageous in facile readout circuits, as most resistive systems use a simple voltage divider compared to the complex circuits required for capacitive sensors, such as capacitance to voltage converters [18]. Voltage divider circuits are less power consuming than their capacitive counterparts, enhancing the ability of the system for long-term motion monitoring. Voltage divider also uses low-cost electronic components, making smart clothing more affordable. In the setting of a multisensor array, the simplicity of the readout circuits, combined with the inherent small footprint of the sensors, enables the design of an ultra-compact electronics system, which is important for the development of smart clothing.

Low-cost textile resistive sensors can be created through the stitching of conductive threads such as silver-plated nylon [19]. The working principle of the textile sensor is that the number of contact points within the stitches decreases as the textile experiences elongating strain, reducing the resistance. As the conductive threads are usually inelastic, the stretchability of the textile sensor comes from the stitch structure including zigzag stitch [20], overlocked stitch [21], and cover stitch [22]. However, the high friction of conductive threads often causes disruptions in the embroidery machine, hindering the scalability of the stitch-based textile sensors [23]. With the recent advancement in nanomaterials, conductive polymer composite (CPC) has gained increasing attention in the area of strain sensing due to its inherent stretchability and ease of fabrication. CPC sensors are often composed of soft elastomers matrix and conductive nanofillers, such as CNT [24] and silver nanowires [25]. Extending from our previous work on ultrathin pressure sensors [26], CPC composed of multi-walled CNT (MWCNT) and thermoplastic PU was (TPU) selected as the strain sensing material. TPU matrix provides great biocompatibility and stretchability, making it suitable for integration with smart clothing. Fabrication methods for TPU/CNT CPC includes dip-coating [27] or spay-coating [28] of TPU fibrous mat with CNT dispersion, and sequential coagulation and compression molding [29]. Interfacial interaction between CNT and TPU within the CPC fabricated through both coating methods are relatively weak, which can lead to the degradation of CNT layer. The detached CNT can cause irritation when in contact with human skin, making it unsuitable for smart clothing [30]. The sequential coagulation and compression molding method produces a relatively large thickness. To overcome these limitations, solvent casts were selected as the fabrication method for their ability to create ultrathin TPU/CNT sensing films with great structural integrity. In addition, the facile fabrication method enables large-scale production of CPC sensors. Although the promising strain sensing capability of TPU/CNT has been documented, its integration into motion monitoring applications remained unreported.

In this article, we target the challenge of multijoint motion estimation in the upper extremities, specifically the estimation of 3-DOF shoulder joint angles and 1-DOF elbow angle. A smart clothing motion monitoring system was developed through the integration of a 10-sensor array composed of TPU/CNT strain sensors. Sensors with different CNT concentrations were fabricated and characterized to determine optimal configuration. The novelty of this article come in two folds: 1) the usage of an alternative low-cost alternative sensing modality, namely TPU/CNT strain sensors, to demonstrate its usefulness when paired with a machine learning algorithm to overcome its limitation; 2) the design of a novel CNN architecture to encode reinforced spatial information in its input and facilitate the simultaneous intra-array and temporal feature extraction. In summary, by prioritizing sensing modality with low power consumption,

Authorized licensed use limited to: The University of Toronto. Downloaded on June 08,2024 at 19:06:41 UTC from IEEE Xplore. Restrictions apply.

This article has been accepted for inclusion in a future issue of this journal. Content is final as presented, with the exception of pagination.

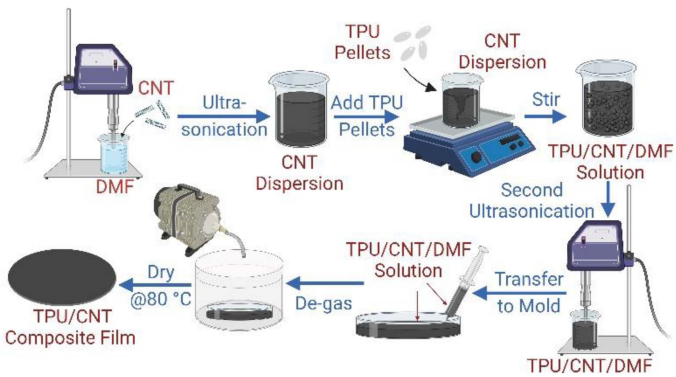

Fig. 1. Fabrication of TPU/CNT sensing film (created with biorender.com).

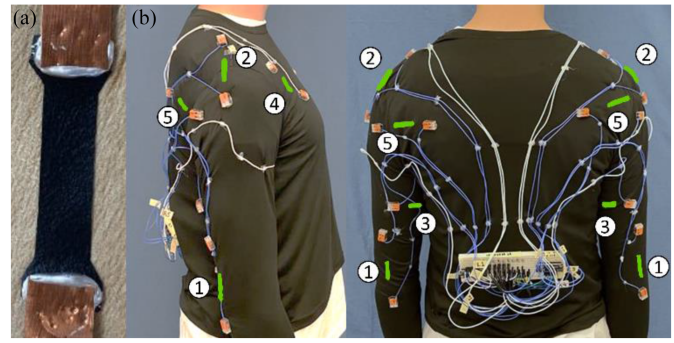

Fig. 2. (a) Complete sensor and (b) complete smart clothing with sensor location indicated in green.

ultrasmall footprint, and scalable fabrication method, we provided a framework for the development of affordable, comfortable smart clothing capable of long-term motion monitoring.

II. Methodology

A. Sensor Fabrication

The TPU/CNT piezoresistive sensing film was fabricated via solvent casting method (see Fig. 1). The process involved the following steps:

1) dispersion of CNTs in N,N-Dimethylformamide (DMF) through ultrasonication for 30 min,
2) gradual addition of TPU pellets to the CNT dispersion with magnetic stirring, followed by overnight mixing,
3) 15 min of ultrasonication,
4) 15 min of degassing in a vacuum chamber to remove air bubbles, and
5) removal of the solvent in an 80-°C oven to produce the TPU/CNT sensing film.

A 2-part syringe was used for transferring the polymer solution to avoid contamination from silicon oils typically present in 3-part syringes. Through this process, TPU/CNT nanocomposite with different CNT concentrations was prepared.

To assemble the TPU/CNT sensing film into sensors, it was cut into dog-bone-shaped specimens, and copper foil electrodes were attached to the ends using silver paste. The dog-bone shape helps reduce stress concentration at the interface between the soft sensing film and the rigid copper electrodes [31]. The reduced regions of the dog-bone-shaped specimens had an average length of 20 mm, width of 5 mm, and thickness of 0.1 mm. Copper wires were soldered to the electrodes to facilitate wiring to the electronic readout system. The complete sensor was shown in Fig. 2(a).

TPU pellets (PEARLBOND 12F75UV) were purchased from Lubrizol Co and dried in an air-circulating oven at 80 °C before use. MWCNTs (NC7000 with an average diameter of 9.5 nm, length of 1.5 μm, specific surface area of 250–300 m^2/g, and volume resistivity of 0.0001 Ω·cm) were purchased from Nanocyl SA. DMF (Certified ACS) was purchased from Fisher Chemical and used as received. The cost of raw materials for each sensor is approximately $0.003 CAD representing a significant reduction compared to our previous work [32], which utilized off-the-shelf CNT ink for conductive coating, costing roughly $1 CAD per sensor.

B. Sensor Test

Conductivity analysis was carried out on 20 mm diameter, 0.1 mm thick disks of the sensing film using a dielectric analyzer (DEA) from Novocontrol Technologies (Alpha-N High Resolution DEA). Input voltage signals with frequencies ranging from 10^{-2} to 10^{2} Hz were applied, and the conductivity at 10^{-2} Hz was used as the direct current conductivity.

Surface and cross-section morphology analysis was performed using scanning electron microscopy (JEOL, JSM-IT100). Cross-sections were obtained by immersing the specimen in liquid nitrogen and fracturing it once it became brittle.

Electromechanical testing was done on the assembled TPU/CNT sensors using a universal tensile testing machine (Instron, MicroTester 5848). Sensor resistance was measured using a Wheatstone Bridge circuit with three equal fixed resistors. The voltage signal across the fixed resistor in the fixed resistor branch, denoted as V_1, and the voltage signal across the fixed resistor in the sensor branch, denoted as V_2, were collected using NI-DAQ-USB 6001. As such, the resistance of the TPU/CNT sensing film, denoted as R, was calculated as follows:

$$R = (V_{in}R') \,/\, (V_1 - V_2 + V_{in}/2) - R' \tag{1}$$

where R' is the resistance of the fixed resistor, which was 68 kΩ for all three fixed resistors, and V_{in} is the supplied voltage.

During the maximum sensing range test, specimens underwent breakage or were strained to 500% at a rate of 5%/s. In the cyclic loading test, the specimens were stretched to 50% strain at 1%/s for ten cycles. In the varying strain rate test, specimens experienced 50% strain at rates of 0.25, 0.5, 1, and 2%/s. To assess the long-term repeatability of the sensor signal, the sensors were subjected to 50% strain for 200 stretch-release cycles at the strain rate of 1%/s.

C. Smart Clothing Design

10 sensors in total were integrated into an off-the-shelf compression shirt to create the smart clothing, which was specifically designed to estimate the angles of the elbow and shoulder joints

Authorized licensed use limited to: The University of Toronto. Downloaded on June 08,2024 at 19:06:41 UTC from IEEE Xplore. Restrictions apply.

This article has been accepted for inclusion in a future issue of this journal. Content is final as presented, with the exception of pagination.

on both the left and right sides of the user. The estimated angles were denoted as $\Theta_{\text{left}}\{e_{\text{left}}, \psi_{\text{left}}, \theta_{\text{left}}, \varphi_{\text{left}}\}$ and $\Theta_{\text{right}}\{e_{\text{right}}, \psi_{\text{right}}, \theta_{\text{right}}, \varphi_{\text{right}}\}$ respectively, with e denoting elbow joint angles, and ψ, θ, φ denoting shoulder joint angles are in the form of Euler angles in Y-X-Y order. To achieve this, strategic sensor locations were chosen, as illustrated in Fig. 2(b). These locations were selected to be perpendicular to the rotational axis of the elbow and perpendicular to lines of nonextension near the shoulder joint. This positioning maximizes elongation based on previous research [4]. In total, ten sensors were utilized for both sides. The readout circuit is composed of a voltage divider for its simplicity. This involves measuring the voltage across a fixed resistor (R') and calculating sensor resistance (R) as follows:

$$R = R' \left(V_{\text{in}} - V_{\text{out}}\right)/V_{\text{out}} \tag{2}$$

where V_{in} is the supplied voltage and V_{out} is the measured voltage across the fixed resistor.

Two Arduino Nanos were used to read the analog output voltage signals from the 10 voltage divider circuits, which were converted to their corresponding resistances using (2). Relative resistance change (RRC) was then calculated for each sensor as follows:

$$\text{RRC} = \left(R - R_o\right)/R_o \tag{3}$$

where R_o is the initial resistance of the sensor, measured before integration into the smart clothing. The RRC signals from the left and right sides, denoted as $R_{\text{left}}\{r_1 \ldots r_5\}$ and $R_{\text{right}}\{r_6 \ldots r_{10}\}$, were transmitted to a PC workstation at 100 Hz through a wired connection.

The readout electronics were glued in the lumbar region of the compression shirt, as shown in Fig. 1(b). 20 gauge wires were used to connect the sensor to the readout circuit. Only a few points on the wires were glued onto the compression shirt, leaving sufficient slack in the wires to not impede motion. The wires were connected to both ends of the sensor using wire connectors. These connectors are glued to the compression shirt to fix the location of the sensor. To reduce the relative motion between the sensors and the compression shirt, the sensors were taped onto the compression shirt at the electrodes.

The power consumption of the readout circuit for our smart clothing motion capture system with 10 sensors is approximately 1 mW, whereas the power consumption for an 8-capacitive sensor system in [13] is approximately 11.34 mW [33]. Moreover, the readout circuit for our smart clothing costs approximately \$0.06 CAD per sensor, whereas the off-the-shelf readout circuit used in [13] costs \$1.84 CAD [33] per sensor.

D. Joint Angle Mapping Model

To establish a relationship between the resistance signals and joint angles, a joint angle mapping model is developed for each side, denoted as functions f and g

$$\Theta_{\text{left}} = f\left(R_{\text{left}}\right) \tag{4}$$

$$\Theta_{\text{right}} = g\left(R_{\text{right}}\right). \tag{5}$$

The concept of posture synergy has gained attention in robotics rehabilitation leading to the development of assistive devices that mimic natural human movements [8]. Posture synergy suggests that natural human movements often involve moving different body segments synergistically, creating distinct patterns [9]. As a result, elbow and shoulder joint angles can carry useful insights for each other as they often move together during activities of daily living, therefore the inclusion of all sensor signals can potentially improve the overall motion monitoring accuracy. To address the time-varying behavior of sensors, signals from previous time steps are included in the input to the CNN. 25 timesteps of resistance signals from five sensors are used as the input to the mapping model. The model uses the following modules in sequence to estimate the joint angles.

1) Creation of an activity image representing the motion; two duplicates of the input signals were created and concatenated to the input ensuring that resistance signals from different sensors are positioned adjacent to one another, increasing spatial understanding.
2) Three 1-D convolutional layers to extract temporal features for each sensor.
3) Two 2-D convolutional layer-max-pooling layer pairs to extract spatial features between neighboring sensors.
4) Three fully connected layers for mapping of joint angles using extracted spatial and temporal features.

The number of hidden units in the first CNN layer was adjusted during hyperparameter turning, and was subsequently doubled after each CNN layer following the convention of "VGG" architecture [34], as shown in Fig. 3. The usage of convolution kernels in the CNN model can attenuate signals in the higher frequency range.

E. Data Collection and Model Training

One healthy male volunteer, age 25, performed various actions wearing the smart clothing, while a vision-based skeleton tracking system simultaneously collected the ground truth joint angle data. Actions including both elbow bending, only left/right elbow bending, row, front raise, jumping jack, lateral raise, and pectoral fly were performed. The volunteer was asked to perform these actions for durations between 1 and 3 min at varying frequencies. An Intel RealSense D455 depth camera was placed approximately 1 m in front of the volunteer to capture depth data. The usage of a depth camera was chosen to enable the portability of the calibration process. In order to extract the volunteer's joint angles, Nuitrack SDK was used for full-body skeletal tracking. Three-dimensional positions of wrist joints, elbow joints, and shoulder joints were used for the computation of ground truth joint angles, denoted as $\Theta'\{e, \psi, \theta, \varphi\}$. The joint angle extraction module outputted Θ'_{left} and Θ'_{right} at 30 Hz. To match the time stamps of the R_{left} and R_{right}, the joint angles were up-sampled via linear interpolation. As such, matching datasets $\{\Theta'_{\text{left}}, R_{\text{left}}\}$ and $\{\Theta'_{\text{right}}, R_{\text{right}}\}$ were created for each action. Both the joint angles and the RRC signals were then filtered using a Butterworth low-pass filter with a cutoff frequency of 5 Hz.

A sliding window method with a window size of 25 and step size of 4 was used on the R to create batches for each action

Authorized licensed use limited to: The University of Toronto. Downloaded on June 08,2024 at 19:06:41 UTC from IEEE Xplore. Restrictions apply.

This article has been accepted for inclusion in a future issue of this journal. Content is final as presented, with the exception of pagination.

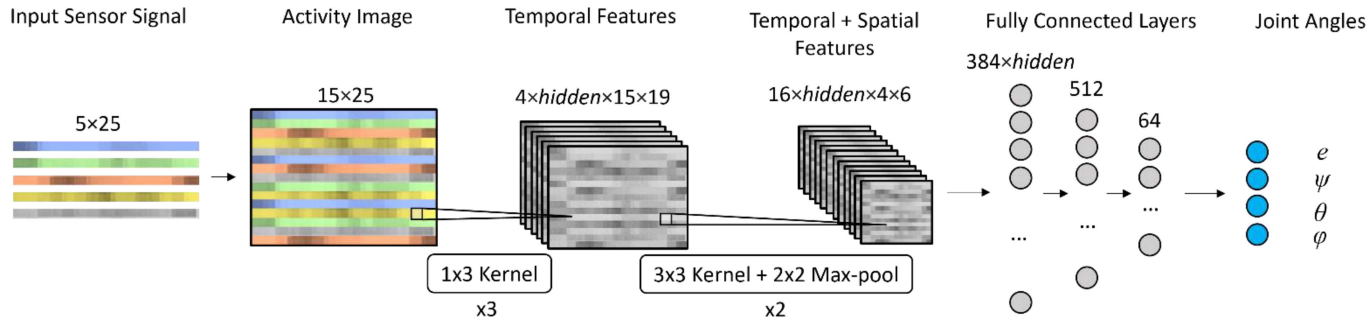

Fig. 3. Architecture of proposed CNN model.

performed and for each left and right side. Each batch of R is matched with a Θ' corresponding to the last timestep.

In conclusion, 24 555 batches of R with matching Θ' combining all actions were created for each side. These batches were then split into a test set, validation set, and training set. The test set is constructed using the last 10% timesteps of each action, and the remaining data is randomized into the training and validation set with a 7:2 ratio. Calibration is accomplished by the training of the networks f and g that aim to minimize the root mean squared error (RMSE) between Θ and Θ'. Training of the model was done by employing the Adam optimizer and using the training set only. Throughout the training process, hyperparameters such as learning rate and model hidden layers are adjusted to minimize the RMSE on the validation set. Hyperparameters including learning rate, batch size, weight decay, and number of hidden layers were tuned based on RMSE evaluated using the validation set. The values of hyperparameters are randomly sampled in desired ranges, and automatically searched within the first ten epochs via Ray Tune [35]. Hyperparameters were tuned separately for the dataset from the left and right sides. Approximately 20 min were required to determine the optimal hyperparameters from 20 combinations of hyperparameters for each side. The tuned hyperparameters were then used for further training of 100 epochs taking approximately 20 min for each size. Models were saved after each epoch, and the model with the lowest validation loss was selected for testing.

III. Results

A. Sensor Properties

To evaluate the effectiveness of the fabrication method, we computed the percolation properties of the fabricated sensing films, namely the percolation threshold, Φ_c, and the percolation component, t. The properties are extracted from the measured conductivity, denoted as σ, from specimens of using different concentrations of CNT, denoted as, Φ. The conductivity of the CPC sensing film is achieved through a network of conductive CNTs embedded in the TPU matrix. At low Φ, there are not enough conductive pathways for the nanocomposite to be conductive. As Φ increases, more conductive pathways are formed, reaching Φ_c where the σ of the nanocomposite increases drastically. During preliminary testing, it was observed that the drastic σ increase occurred between 2 and 2.5 wt% CNT. The σ–Φ curve was plotted and shown in Fig. 4(a). According to

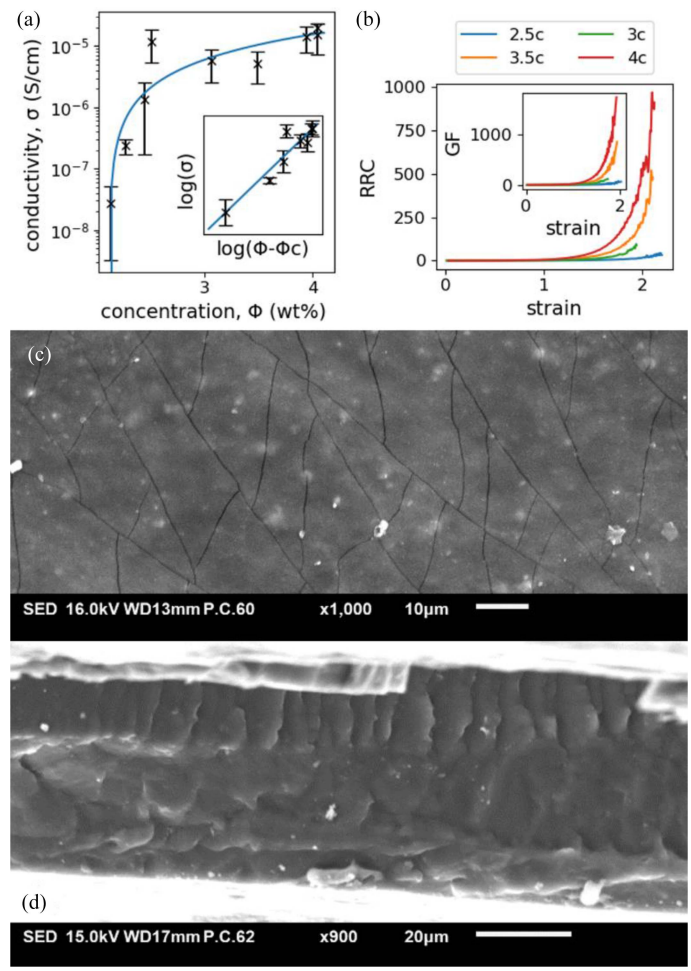

Fig. 4. (a) Curve fitting of experimental conductivity data to percolation theory (inset of linearized curve). (b) RRC showed an exponential increase when subjected to increasing strain (inset of gauge factor). (c) SEM image of specimen 4C and cracks on the surface. (d) SEM of the cross-sectional view of cracks of specimen 4C.

percolation theory, the relationship between the σ and Φ can be described in the following equation:

$$\sigma = \sigma_o(\Phi - \Phi_c)^t \tag{7}$$

where σ_0 is a fitted constant proportional to the conductive property of the filler. The fitted curve representing (1) as shown in Fig. 4(a) yielded $\Phi c = 2.125$ wt%, $\sigma_0 = 7.05 \times 10^{-6}$ S/cm, and

Authorized licensed use limited to: The University of Toronto. Downloaded on June 08,2024 at 19:06:41 UTC from IEEE Xplore. Restrictions apply.

This article has been accepted for inclusion in a future issue of this journal. Content is final as presented, with the exception of pagination.

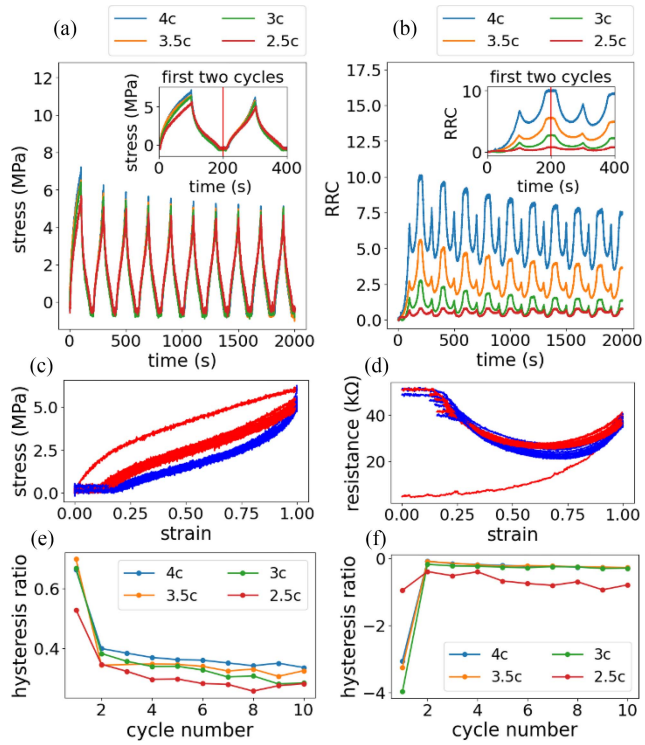

Fig. 5. (a) Stress-time curve from cyclic loading test. (b) RRC-time curve from cyclic loading test. (c) Example stress versus strain curve of specimen 2.5C. (d) Example resistance versus strain curve of specimen 4C. (e) and (f) Mechanical and electromechanical hysteresis ratio for each cycle.

$t = 1.25$. The value of Φc is estimated by choosing the value that allowed for the best linear fitting ($R^2 = 0.884$) of $\log(\sigma)$ and $\log(\Phi - \Phi c)$, shown in the inset of Fig. 4(a).

Specimens with CNT concentration higher than the percolation threshold, specifically 2.5, 3, 3.5, and 4 wt%, denoted as 2.5C, 3C, 3.5C, and 4C, respectively, were then fabricated and further characterized. First, the maximum sensing range test was conducted. The RRC-strain curve was plotted and shown in Fig. 4(b). The sensitivity of the specimen in the form of gauge factor (GF) was calculated as follows:

$$\mathrm{GF} = d\,(\mathrm{RRC})\,/d\varepsilon \tag{8}$$

where $d\varepsilon$ is the incremental strain, and $d(\mathrm{RRC})$ indicates the incremental change of RRC. The RRC-strain curves of the example specimens from each of 2.5C, 3C, 3.5C, and 4C were plotted and shown in Fig. 4(b), and the derived GF-strain curves were shown in the inset of Fig. 4(b).

To investigate the macro-structural damage done to the specimen during the maximum sensing range test, surface and cross-sectional morphology analysis was done on the post-test specimens. SEM images of the surface and cross-section of 4C were shown in Fig. 4(c) and (d), respectively.

The macro-structural damage was further studied by subjecting the specimens to cyclic loading. The stress-time curves of the example specimens from each of 2.5C, 3C, 3.5C, and 4C were plotted and shown in Fig. 5(a), and the RRC-time curves of the example specimens from each of 2.5C, 3C, 3.5C, and 4C

TABLE I
MECHANICAL HS, ELECTRICAL HS, AND GF

Name	Mechanical HS	Electrical HS	GF
4C	0.360±0.023	-0.216±0.059	4.369±1.035
3.5C	0.332±0.014	-0.214±0.057	2.529±0.409
3C	0.323±0.034	-0.247±0.038	1.004±0.271
2.5C	0.292±0.027	-0.658±0.187	0.347±0.160

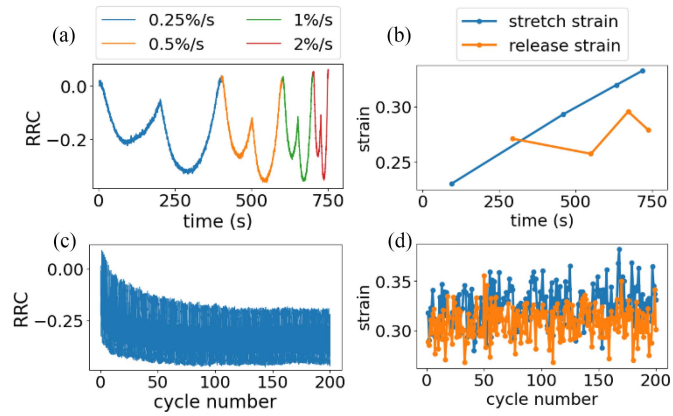

Fig. 6. (a) 4C resistance signals when subjected to various strain rate. (b) Strain of negative-to-positive Piezoresistivity switch during varying strain rate test. (c) 4C resistance signals during long term repeatability test. (d) Strain of negative-to-positive Piezoresistivity switch during long term repeatability.

were plotted and shown in Fig. 5(b). The stress-strain curve of 2.5C specimen was plotted and shown in Fig. 5(c), with loading and unloading regions represented in red and blue, respectively. The mechanical hysteresis ratio (HS) can be calculated from the stress–strain curves

$$\mathrm{HS} = (A_{\mathrm{loading}} - A_{\mathrm{unloading}})/A_{\mathrm{loading}} \times 100\% \tag{9}$$

where A_{loading} and $A_{\mathrm{unloading}}$ are areas under the loading and unloading curves, respectively. The mechanical HS was calculated for each cycle, and the HS-cycle curves were plotted in Fig. 5(c). The resistance-strain curve of 4C specimen was plotted and shown in Fig. 5(d). Similarly, electric hysteresis was evaluated using (5), and the HS-cycle curves plotted in Fig. 5(f).

Mechanical HS, electrical HS, and GF were collected from 5 samples for each CNT concentration, and the results were summarized in Table I. GF was calculated using the data from the first loading cycle in a cyclic loading test via linear fitting.

Due to the consistent resistance response during dynamic loading conditions and higher sensitivity, specimens with 4 wt% CNT were chosen to be integrated into smart clothing, and their sensing properties were further investigated. The electromechanical response stabilized after repeated stretch-release cycles, so all integrated and tested sensors were pretreated with cyclic stretching up to 100% strain for 10 cycles. To simulate practical scenarios, one pretreated 4C specimen was subjected to a varying strain rate test. The RRC-time curve was plotted and shown in Fig. 6(a). As observed, the piezoresistivity switched from negative to positive during loading, and vice-versa during

Authorized licensed use limited to: The University of Toronto. Downloaded on June 08,2024 at 19:06:41 UTC from IEEE Xplore. Restrictions apply.

This article has been accepted for inclusion in a future issue of this journal. Content is final as presented, with the exception of pagination.

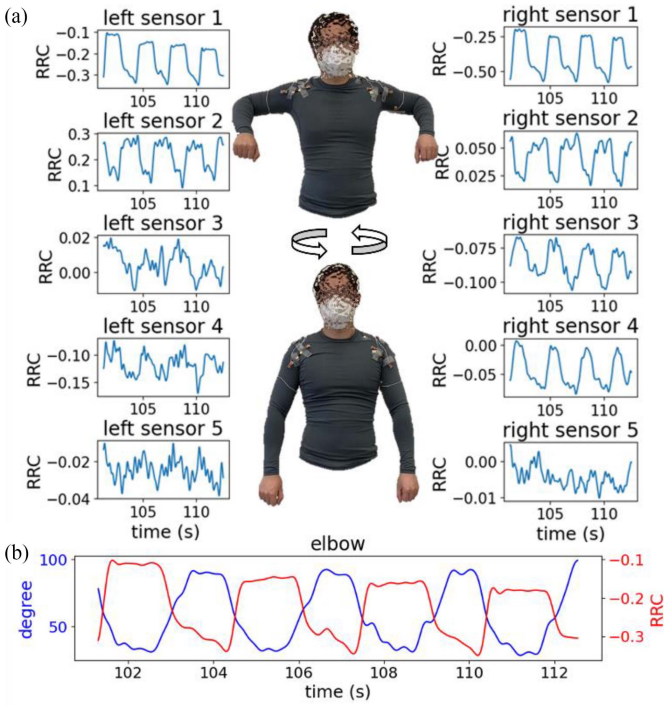

Fig. 7. (a) Raw resistance signals from repetitive rowing actions. (b) Raw resistance signal from left sensor 1 and left elbow bending angle.

unloading. The switch strain was obtained by finding the minimum RRC in each half cycle and matching its corresponding strain, and the switch strain-time curves were plotted in Fig. 6(b). Subsequently, the long-term repeatability test was conducted. The RRC-cycle number curves were plotted and shown in Fig. 6(c), and similarly, the switch strain-cycle number points were plotted in Fig. 6(d). Ten 4C sensors were fabricated and integrated into the smart clothing, with sensors having a mean resistance of 214.6 kΩ and a standard deviation of 165.1 kΩ.

B. Motion Monitoring Performance

Fig. 7(a) depicted RRC signals in the portion of the test set where the volunteer performed four repetitions of rowing action, and distinct cyclic patterns were evident. A mainly negative correlation was observed between the right elbow bending angle and the RRC signal from right sensor 1, as shown in Fig. 7(b), consistent with the sensor testing results. It is worth noting that in Fig. 7(a) L sensor 2, R sensor 2, and L sensor 3 showed positive RRC values while the rest of the RRC values remained negative. This is attributed to the incomplete rearrangement of the conductive pathways during the prestretching process, causing the sensor resistance to increase further after integration leading to larger resistance values than R_0, thus the positive RRC values. However, the conductive pathways in L sensor 2, R sensor 2, and L sensor 3 quickly stabilized and consistent negative piezoresistivity was observed. In addition, the observed variation in the noise magnitude of the raw sensor signals is attributed to the nominal resistance variability among the sensors. The larger disparity between the sensor resistance and the reference resistance in the readout electronics contributes to an increased magnitude of sensor signal noise.

The performance of the joint angle mapping model is evaluated by computing the normalized RMSE (NRMSE) and the R2 value between Θ, and Θ' in the test set. As each joint underwent different ranges of motion, NRMSE is more indicative of relative motion monitoring performance between different monitored joints. NRMSE was calculated by dividing the RMSE by the range of each joint angle in the test set. Overall R2 values between Θ and Θ' were calculated to be {0.911,0.767,0.830,0.919} and {0.925,0.834,0.847,0.915} for the left and right sides, respectively. NRMSE for each action, presented in percentage, was summarized in Table II. Comparison between ground truth and model output joint angles in the test set was shown in Fig. 8. Different actions in Fig. 8 were separated by a vertical red line and were plotted in the following order: both elbows bending, front raise, left elbow bending, jumping jack, lateral raise, row, right elbow bending, and pectoral fly. The maximum absolute error for each estimated joint was summarized in Table III. Our smart clothing motion monitoring system was able to output the eight estimated joint angles at 50 Hz using a PC workstation with NVIDIA GeForce GTX 1060 6GB GPU and Intel Core i7-8700 CPU.

IV. Discussion

A. Sensor

The percolation exponent (t) indicates the dimensionality of the percolation network, which is 2-D for 3-D networks according to classical percolation theory [36]. With the value of t typically ranging from 0.5 to 7 in the literature, our fitted value showed similarity to that of other CNT-based CPCs [29], [36], [37]. The relatively high percolation threshold in this design is attributed to reagglomeration during the drying process [38]. Having a higher percolation threshold indicates a higher amount of CNT required to produce functional sensing material, which leads to stronger yield strength. Such limitation can be addressed by increasing drying temperature reduces evaporation time, which in turn reduces reagglomeration. The effect of drying temperature will be investigated in future studies.

The tunneling effect model describes an exponential increase in RRC when the specimen is subjected to an increasing strain [39], explaining the RRC-strain curve observed in Fig. 4(b). As shown in Fig. 4(c) and (d), cracks and damage were observed on the surface and cross-section of specimens with higher CNT content. It was apparent from Table I that higher CNT wt% correlates to higher sensitivity, contradictory to observations made in other studies where higher CNT wt% resulted in lower CNT concentrations due to the abundance of conductive pathways [40], [41]. In this study, the higher sensitivity at higher CNT concentration can be explained by the increased macrostructural damage to the nanocomposite at higher CNT wt%, as indicated by the positive correlation between CNT wt% and mechanical HS, and higher mechanical HS indicates a higher degree of macrostructural damage [42].

The stress response shown in Fig. 5(a) displayed greater stress during the first cycle, indicating the formation of cracks. Flat

Authorized licensed use limited to: The University of Toronto. Downloaded on June 08,2024 at 19:06:41 UTC from IEEE Xplore. Restrictions apply.

This article has been accepted for inclusion in a future issue of this journal. Content is final as presented, with the exception of pagination.

TABLE II
NRMSE OF EACH MEASURED JOINT FOR DIFFERENT ACTIONS

Action name	Left				Right			
	e	ψ	θ	φ	e	ψ	θ	φ
Elbows bending	9.04	3.99	3.97	5.00	7.75	3.30	2.91	2.61
Front raise	5.32	9.85	10.18	9.98	4.51	7.43	7.01	9.67
Left elbow bending	5.48	7.59	4.97	7.46	5.93	5.46	1.50	3.17
Jumping Jack	9.61	6.70	5.31	9.68	6.62	5.60	5.53	8.95
Lateral raise	3.40	8.39	7.29	8.87	4.14	6.00	6.22	9.49
Row	4.68	6.26	5.26	5.87	11.94	5.87	3.19	11.71
Right elbow bending	2.70	2.98	1.37	1.63	5.24	5.18	4.78	3.80
Pectoral fly	4.20	13.72	11.84	5.22	4.28	13.14	11.22	7.10
All actions	6.82	7.80	6.83	8.12	6.71	6.57	5.78	8.37

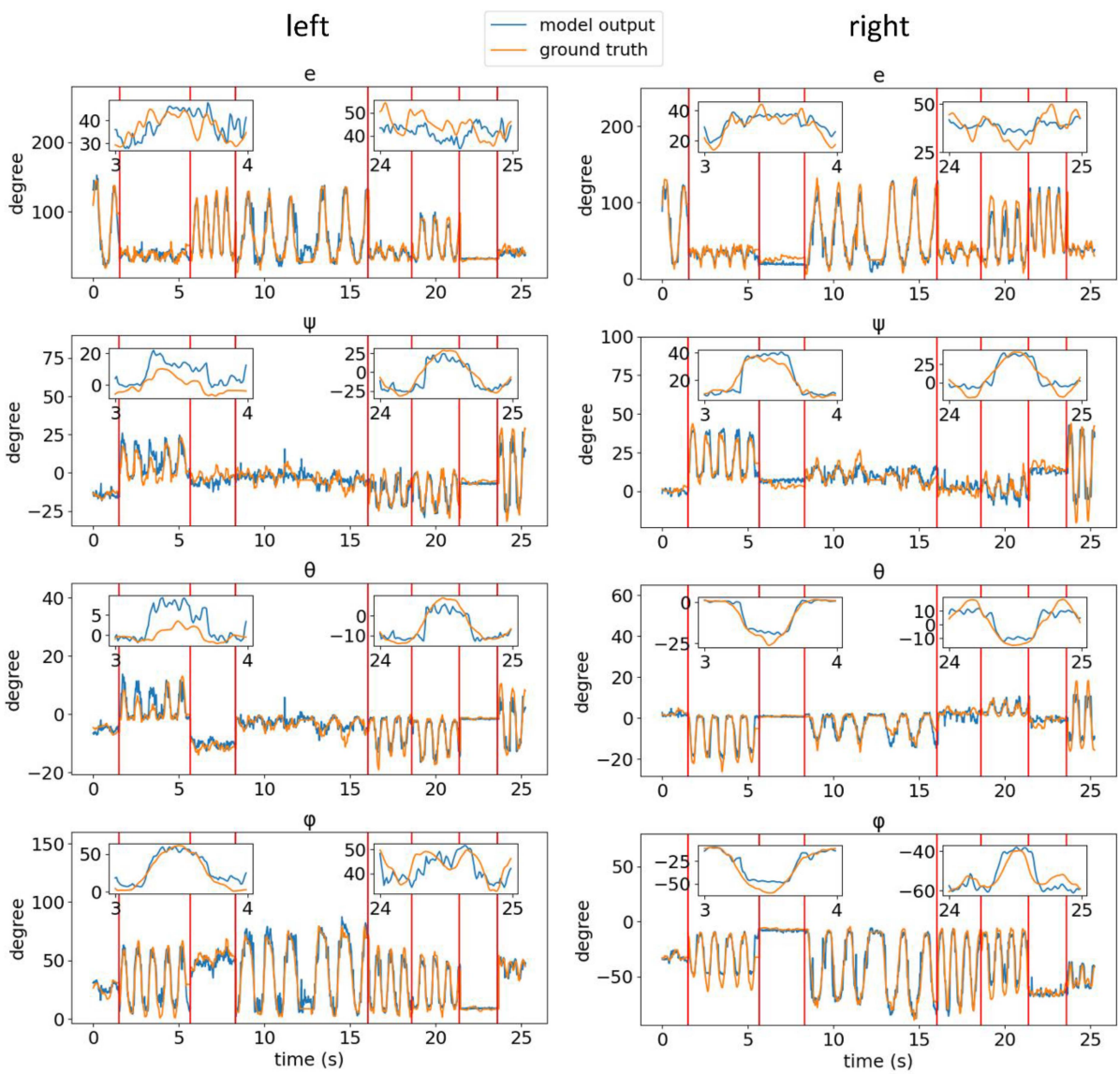

Fig. 8. Comparison of ground truth and model output.

Authorized licensed use limited to: The University of Toronto. Downloaded on June 08,2024 at 19:06:41 UTC from IEEE Xplore. Restrictions apply.

This article has been accepted for inclusion in a future issue of this journal. Content is final as presented, with the exception of pagination.

TABLE III
MAXIMUM ABSOLUTE ERRORS FOR EACH MEASURED JOINT

Left	Left	Left	Left	Right	Right	Right	Right
e	ψ	θ	φ	e	ψ	θ	φ
51.70	23.56	11.01	32.62	48.14	16.20	10.16	35.48

regions were observed in subsequent cycles, indicating plastic deformation of the specimens. As shown in Fig. 5(e), the mechanical hysteresis ratio decays after cyclic loading, indicating a more stable macrostructure. Resistance signals collected during cyclic loading showed a permanent increase in resistance after the first cycle, indicating that crack formation prevented the conductive CNT network from returning to its original state, resulting in permanent changes in electromechanical behavior. However, in the subsequent cycles, the electromechanical behavior became consistent, showing a stabilized conductive network in the newly damaged macro-structure. Interestingly, during the initial release, the resistance first decreased and then increased to the highest level. This phenomenon finds its explanation in the stress state experienced by the nanocomposite. When stretched, the tensile stress caused the conductive pathways formed by CNTs to break apart in the axial direction, while the transverse compressive stress pushed the CNT closer, creating new conductive pathways. Then, during the release phase, the axial recovery only partially reconstructed the conductive pathways due to crack formation, resulting in an initial decrease in resistance. In contrast, the specimen underwent a higher degree of recovery in the transverse direction, causing a net destruction of the conductive pathways and a subsequent increase in resistance to the highest level. Furthermore, in the subsequent cycles, a double peak phenomenon was observed, which is consistent with other studies utilizing TPU/CNT nanocomposites for strain sensing [43], [44], [45]. This phenomenon is commonly attributed to the competition of destruction and reconstruction of conductive pathways, with our observation highlighting the impact of the macro-structural damage. It was also observed that a faster strain rate delayed the piezoresistivity switch, suggesting that the faster strain rate aided the reconstruction of conductive pathways.

As shown in Fig. 6(c), the raw resistance of the sensor decayed and stabilized after approximately 100 cycles. The decay of the resistance was mainly attributed to the relaxation of polymer chains in viscoelastic materials [43], as well as the alignment of CNT along the stretch direction [40]. The piezoresistivity-switch strain during the 200 stretch-release cycles showed that the switch strain in the release cycle was generally lower than in the stretch cycle, as shown in Fig. 6(d). This observation, coupled with the more rapid decrease in tensile stress during release cycles, indicated that the presence of tensile stress aided the destruction of conductive pathways.

B. Smart Clothing System

No significant deviation was observed between the same angles on different sides. However, for shoulder Euler angles, NRMSE of θ was smaller than that of ψ and φ in most actions. This is attributed to θ causing singularity in the first (ψ) and third (φ) rotation axes when it approaches zero; when the first and third axes are approaching singularity, multiple values for ψ and φ will be valid, causing the joint angle extraction module to output inconsistent values for ψ and φ, leading to larger error. A similar observation was reported in other work utilizing Euler angles [13], which is a limitation presented by the choice of shoulder angle representation. Alternative shoulder joint representation, such as angles of the projected humerus on sagittal, frontal, and transverse planes, may offer potential improvements to the motion monitoring accuracy.

Front raise and pectoral fly produced the largest overall error for shoulder angle estimations. This can be attributed to the limitation of the depth camera-based skeleton tracking system. The extracted joint angles became increasingly noisy when the volunteer's arms approached positions pointing directly at the camera, as less depth data could be captured by the camera. Both front raise and pectoral fly involved moving arms towards such positions. This limitation can be overcome by using a multicamera system with the tradeoff of losing portability. The three sets of actions that isolated elbow motion produced the largest overall error for e, and the lowest error for shoulder angles. In general, the different overall error produced by different actions suggests that errors were higher for actions, which produces large joint angles.

In addition, significant maximum absolute errors were recorded. The largest error commonly occurred at peaks of the joint angles, such as left and right ψ between timestep 2300 and 2500 during pectoral fly, right θ between timestep 2300 and 2500 during pectoral fly, left θ between timestep 1650 and 1700 during front raise, and right e between timestep 1900 and 2000 during the row. This is attributed to the higher degrees of nonlinearity of the sensors at larger strains, making it more challenging for the model to extract the relationship between R and Θ in these regions. To facilitate the training to focus more on the peaks on the angles, the loss function can be adjusted such that deviation between Θ and Θ' and penalized severely at high values of ground truth joint angles. The largest error for left e and φ occurred between timesteps 1200 and 1300 during jumping jack where the volunteer took a pause between the repetitions. This can be attributed to the model prediction of increasing joint angles based on the previous timesteps, which suggests the limitation of the model to accurately extract temporal features. Recurrent neural network layers may be utilized in addition to CNN layers to better extract temporal features. Finally, the maximum absolution error in right φ between timestep 1100 and 1200 during pectoral fly could also be caused by a large spike of noise in the sensor signals. A more secure integration method such as sewing can improve the sensor signal quality. The current integration approach is

Authorized licensed use limited to: The University of Toronto. Downloaded on June 08,2024 at 19:06:41 UTC from IEEE Xplore. Restrictions apply.

This article has been accepted for inclusion in a future issue of this journal. Content is final as presented, with the exception of pagination.

susceptible to occasional slippage between the sensor ends and the smart clothing due to partial tape adhesion loss. This slippage leads to an incomplete transfer of strain from the smart clothing fabric to the sensor, introducing additional errors in the sensor signal. Alternatively, other methods involve adopting a sewable form factor for the sensor and employing embroidery techniques to secure the sensor attachment [23], effectively eliminating relative movement between the sensor and the fabric. Nevertheless, additional research is required to tailor embroidery equipment for the specific needs of processing soft sensing threads.

A previous study [46] presented the development of smart clothing that utilized fourteen commercially available resistive sensors to measure shoulder joint angles and elbow bending angles. The average RMSE for elbow angles was reported as 12.65°, and for shoulder angles were 7.31°, 10.21°, and 15.45° in their work. In contrast, using only ten sensors, the performance of our smart clothing system represented a significant improvement of 5.81° in RMSE for each measure joint on average. To the authors' knowledge, the article [46] is the only known study that has attempted to estimate both elbow and shoulder angles simultaneously. However, the ability of our smart clothing to accurately monitor motion for multiple users was not evaluated. Future work will focus on multiuser studies to investigate usability and inter-user performance.

V. Conclusion

In this article, we have presented the development of a motion-capturing smart clothing system, from the design and fabrication of the TPU/CNT strain sensors to the development of the CNN-based mapping algorithm. Strain sensors with 4 wt% CNT demonstrated the best signal consistency and sensitivity. GF of 4.369 was achieved in the range of below 100% strain. It was concluded that the higher sensitivity was related to the higher level of microstructural damage, indicated by the higher mechanical hysteresis ratio. The double peak phenomenon was investigated, and the cause was attributed to the combination of the alignment of CNT. A joint angle mapping model was developed based on a novel CNN architecture, to extract intra-array correlation and temporal features simultaneously. Motion monitor performance for elbow bending, front raise, jumping jack, lateral raise, row, and pectoral fly was evaluated, and overall NRMSEs of 6.77%, 7.19%, 6.31%, and 8.22% were obtained for elbow angle, e, and shoulder Euler angles, ψ, θ, φ, respectively. No noticeable inter-array deviation in performance was observed. Our prototype provides a strong basis for the advancement of low-cost wearable motion-capturing systems. In addition to providing quantitative measurements of upper limb motions, the output of the smart clothing system can be used to construct skeleton information of the user, enabling multimodal sensor fusion with skeleton information received from camera-based systems and IMU-based systems, benefitting high-level recognition tasks such as activity classification and user affect estimation. By integrating piezoresistive sensors and simple readout electronics, we aim to increase the use of smart clothing-based motion monitoring technology.

Acknowledgment

The authors would like to thank S. M. Taromsari, D. Anastasia Aubeeluck, and A. Hao Tan for their support in the completion of this article.

References

[1] S. Das et al., "Quantitative measurement of motor symptoms in Parkinson's disease: A study with full-body motion capture data," in *Proc. Annu. Int. Conf. IEEE Eng. Med. Biol. Soc.*, 2011, pp. 6789–6792, doi: 10.1109/IEMBS.2011.6091674.

[2] N. Eichler, H. Hel-Or, I. Shimshoni, D. Itah, B. Gross, and S. Raz, "3D motion capture system for assessing patient motion during Fugl-Meyer stroke rehabilitation testing," *Inst. Eng. Technol. Comput. Vis.*, vol. 12, no. 7, pp. 963–975, 2018, doi: 10.1049/iet-cvi.2018.5274.

[3] A. M. Sabatini, "Estimating three-dimensional orientation of human body parts by inertial/magnetic sensing," *Sensors*, vol. 11, no. 2, pp. 1489–1525, Feb. 2011, doi: 10.3390/s110201489.

[4] D. Álvarez, J. C. Alvarez, R. C. González, and A. M. López, "Upper limb joint angle measurement in occupational health," *Comput. Methods Biomech. Biomed. Eng.*, vol. 19, no. 2, pp. 159–170, Jan. 2016, doi: 10.1080/10255842.2014.997718.

[5] J. Cockcroft, J. H. Muller, and C. Scheffer, "A novel complimentary filter for tracking hip angles during cycling using wireless inertial sensors and dynamic acceleration estimation," *IEEE Sensors J.*, vol. 14, no. 8, pp. 2864–2871, Aug. 2014, doi: 10.1109/JSEN.2014.2318897.

[6] E. Ruffaldi, L. Peppoloni, A. Filippeschi, and C. A. Avizzano, "A novel approach to motion tracking with wearable sensors based on probabilistic graphical models," in *Proc. IEEE Int. Conf. Robot. Autom.*, 2014, pp. 1247–1252, doi: 10.1109/ICRA.2014.6907013.

[7] E. R. Bachmann, X. Yun, and C. W. Peterson, "An investigation of the effects of magnetic variations on inertial/magnetic orientation sensors," in *Proc. IEEE Int. Conf. Robot. Autom.*, 2004, vol. 2, pp. 1115–1122, doi: 10.1109/ROBOT.2004.1307974.

[8] M. Amjadi, K.-U. Kyung, I. Park, and M. Sitti, "Stretchable, skin-mountable, and wearable strain sensors and their potential applications: A review," *Adv. Funct. Mater.*, vol. 26, no. 11, pp. 1678–1698, 2016, doi: 10.1002/adfm.201504755.

[9] M. Gholami, A. Ejupi, A. Rezaei, A. Ferrone, and C. Menon, "Estimation of knee joint angle using a fabric-based strain sensor and machine learning: A preliminary investigation," in *Proc. 7th IEEE Int. Conf. Biomed. Robot. Biomechatronics*, 2018, pp. 589–594, doi: 10.1109/BIOROB.2018.8487199.

[10] Y. Feng et al., "Dynamic measurement of legs motion in sagittal plane based on soft wearable sensors," *J. Sensors*, vol. 2020, Feb. 2020, Art. no. e9231571, doi: 10.1155/2020/9231571.

[11] H. Park, J. Cho, J. Park, Y. Na, and J. Kim, "Sim-to-real transfer learning approach for tracking multi-DOF ankle motions using soft strain sensors," *IEEE Robot. Autom. Lett.*, vol. 5, no. 2, pp. 3525–3532, Apr. 2020, doi: 10.1109/LRA.2020.2979631.

[12] M. Gholami, A. Rezaei, T. J. Cuthbert, C. Napier, and C. Menon, "Lower body kinematics monitoring in running using fabric-based wearable sensors and deep convolutional neural networks," *Sensors*, vol. 19, no. 23, Jan. 2019, Art. no. 5325, doi: 10.3390/s19235325.

[13] Y. Jin et al., "Soft sensing shirt for shoulder kinematics estimation," in *Proc. IEEE Int. Conf. Robot. Autom.*, 2020, pp. 4863–4869, doi: 10.1109/ICRA40945.2020.9196586.

[14] H. Nakamoto, H. Ootaka, M. Tada, I. Hirata, F. Kobayashi, and F. Kojima, "Stretchable strain sensor based on areal change of carbon nanotube electrode," *IEEE Sensors J.*, vol. 15, no. 4, pp. 2212–2218, Apr. 2015, doi: 10.1109/JSEN.2014.2377022.

[15] A. Atalay et al., "Batch fabrication of customizable silicone-textile composite capacitive strain sensors for human motion tracking," *Adv. Mater. Technol.*, vol. 2, no. 9, 2017, Art. no. 1700136, doi: 10.1002/admt.201700136.

[16] B. Oldfrey, R. Jackson, P. Smitham, and M. Miodownik, "A deep learning approach to non-linearity in wearable stretch sensors," *Front. Robot. AI*, vol. 6, 2019, Art. no. 409067.

[17] D. S. Wood et al., "Accurate prediction of knee angles during open-chain rehabilitation exercises using a wearable array of nanocomposite stretch sensors," *Sensors*, vol. 22, no. 7, Jan. 2022, Art. no. 2499, doi: 10.3390/s22072499.

Authorized licensed use limited to: The University of Toronto. Downloaded on June 08,2024 at 19:06:41 UTC from IEEE Xplore. Restrictions apply.

This article has been accepted for inclusion in a future issue of this journal. Content is final as presented, with the exception of pagination.

[18] D. Xu, T. G. McKay, S. Michel, and I. A. Anderson, "Enabling large scale capacitive sensing for dielectric elastomers," in *Proc. Electroactive Polym. Actuators Devices*, 2014, pp. 269–276, doi: 10.1117/12.2044356.

[19] O. Tangsirinaruenart and G. Stylios, "A novel textile stitch-based strain sensor for wearable end users," *Materials*, vol. 12, no. 9, Jan. 2019, Art. no. 1469, doi: 10.3390/ma12091469.

[20] M. Martínez-Estrada, I. Gil, and R. Fernández-García, "An alternative method to develop embroidery textile strain sensors," *Textiles*, vol. 1, no. 3, pp. 504–512, Dec. 2021, doi: 10.3390/textiles1030026.

[21] G. Gioberto, C. Compton, and L. Dunne, "Machine-stitched E-textile stretch sensors," *Sensors Transducers J.*, vol. 202, pp. 25–37, Jul. 2016, doi: 10.13140/RG.2.2.23283.68644.

[22] R. I. Ramos-Garcia, F. Da Silva, Y. Kondi, E. Sazonov, and L. E. Dunne, "Analysis of a coverstitched stretch sensor for monitoring of breathing," in *Proc. 10th Int. Conf. Sens. Technol.*, 2016, pp. 1–6, doi: 10.1109/ICSensT.2016.7796258.

[23] J. G. C. Alfaro and A. L. Trejos, "Design and fabrication of embroidered textile strain sensors: An alternative to stitch-based strain sensors," *Sensors*, vol. 23, no. 3, Jan. 2023, Art. no. 1503, doi: 10.3390/s23031503.

[24] T. N. Lam et al., "Microfluidic preparation of highly stretchable natural rubber microfiber containing CNT/PEDOT: PSS hybrid for fabric-sewable wearable strain sensor," *Composites Sci. Technol.*, vol. 210, Jul. 2021, Art. no. 108811, doi: 10.1016/j.compscitech.2021.108811.

[25] M. Amjadi, A. Pichitpajongkit, S. Lee, S. Ryu, and I. Park, "Highly stretchable and sensitive strain sensor based on silver nanowire-elastomer nanocomposite," *Amer. Chem. Soc. Nano*, vol. 8, no. 5, pp. 5154–5163, May 2014, doi: 10.1021/nn501204t.

[26] D. A. Aubeeluck, C. Forbrigger, S. M. Taromsari, T. Chen, E. Diller, and H. E. Naguib, "Screen-printed resistive tactile sensor for monitoring tissue interaction forces on a surgical magnetic microgripper," *Amer. Chem. Soc. Appl. Mater. Interfaces*, vol. 15, no. 28, pp. 34008–34022, Jul. 2023, doi: 10.1021/acsami.3c04821.

[27] W. Wang et al., "Double-layered conductive network design of flexible strain sensors for high sensitivity and wide working range," *Amer. Chem. Soc. Appl. Mater. Interfaces*, vol. 14, no. 32, pp. 36611–36621, Aug. 2022, doi: 10.1021/acsami.2c08285.

[28] Y. Zhou et al., "Significant stretchability enhancement of a crack-based strain sensor combined with high sensitivity and superior durability for motion monitoring," *Amer. Chem. Soc. Appl. Mater. Interfaces*, vol. 11, no. 7, pp. 7405–7414, Feb. 2019, doi: 10.1021/acsami.8b20768.

[29] I. V. Novikov et al., "Multifunctional elastic nanocomposites with extremely low concentrations of single-walled carbon nanotubes," *Amer. Chem. Soc. Appl. Mater. Interfaces*, vol. 14, no. 16, pp. 18866–18876, Apr. 2022, doi: 10.1021/acsami.2c01086.

[30] G. Acar, O. Ozturk, A. J. Golparvar, T. A. Elboshra, K. Böhringer, and M. K. Yapici, "Wearable and flexible textile electrodes for biopotential signal monitoring: A review," *Electronics*, vol. 8, no. 5, p. 479, May 2019, doi: 10.3390/electronics8050479.

[31] L. A. García-García, J. C. Costa, P. Lugoda, D. Roggen, and N. Münzenrieder, "Copper wire based electrical contacts for direct interfacing of stretchable sensors," in *Proc. IEEE Sensors*, 2020, pp. 1–4, doi: 10.1109/SENSORS47125.2020.9278749.

[32] F. Robinson, Z. Cen, H. Naguib, and G. Nejat, "Socially assistive robotics and wearable sensors for intelligent user dressing assistance," in *Proc. 31st IEEE Int. Conf. Robot Hum. Interactive Commun.*, 2022, pp. 829–836, doi: 10.1109/RO-MAN53752.2022.9900778.

[33] "FDC2214 data sheet, product information and support | TI.com," Accessed: May 18, 2023. [Online]. Available: https://www.ti.com/product/FDC2214#order-quality

[34] K. Simonyan and A. Zisserman, "Very deep convolutional networks for large-scale image recognition," 2014, *arXiv:1409.1556*, doi: 10.48550/arXiv.1409.1556.

[35] R. Liaw, E. Liang, R. Nishihara, P. Moritz, J. E. Gonzalez, and I. Stoica, "Tune: A research platform for distributed model selection and training," 2018, *arXiv:1807.05118*, doi: 10.48550/arXiv.1807.05118.

[36] W. Bauhofer and J. Z. Kovacs, "A review and analysis of electrical percolation in carbon nanotube polymer composites," *Composites Sci. Technol.*, vol. 69, no. 10, pp. 1486–1498, Aug. 2009, doi: 10.1016/j.compscitech.2008.06.018.

[37] M. T. Innocent et al., "Piezoresistive fibers with large working factors for strain sensing applications," *Amer. Chem. Soc. Appl. Mater. Interfaces*, vol. 15, no. 1, pp. 2277–2288, Jan. 2023, doi: 10.1021/acsami.2c19830.

[38] G. Mittal, V. Dhand, K. Y. Rhee, S.-J. Park, and W. R. Lee, "A review on carbon nanotubes and graphene as fillers in reinforced polymer nanocomposites," *J. Ind. Eng. Chem.*, vol. 21, pp. 11–25, Jan. 2015, doi: 10.1016/j.jiec.2014.03.022.

[39] X. Wang, X. Liu, and D. W. Schubert, "Highly sensitive ultrathin flexible thermoplastic polyurethane/carbon black fibrous film strain sensor with adjustable scaffold networks," *Nano-Micro Lett.*, vol. 13, no. 1, p. 64, Jan. 2021, doi: 10.1007/s40820-021-00592-9.

[40] X. Chen et al., "Flexible strain sensors with enhanced sensing performance prepared from biaxially stretched carbon nanotube/thermoplastic polyurethane nanocomposites," *Amer. Chem. Soc. Appl. Electron. Mater.*, vol. 4, no. 6, pp. 3071–3079, Jun. 2022, doi: 10.1021/acsaelm.2c00471.

[41] J. Tang, Y. Wu, S. Ma, T. Yan, and Z. Pan, "Flexible strain sensor based on CNT/TPU composite nanofiber yarn for smart sports bandage," *Composites B, Eng.*, vol. 232, Mar. 2022, Art. no. 109605, doi: 10.1016/j.compositesb.2021.109605.

[42] B. Li et al., "A highly stretchable, super-hydrophobic strain sensor based on polydopamine and graphene reinforced nanofiber composite for human motion monitoring," *Composites B, Eng.*, vol. 181, Jan. 2020, Art. no. 107580, doi: 10.1016/j.compositesb.2019.107580.

[43] Z. Zhang et al., "Electromechanical performance of strain sensors based on viscoelastic conductive composite polymer fibers," *Amer. Chem. Soc. Appl. Mater. Interfaces*, vol. 14, no. 39, pp. 44832–44840, Oct. 2022, doi: 10.1021/acsami.2c12120.

[44] J. F. Christ, N. Aliheidari, P. Pötschke, and A. Ameli, "Bidirectional and stretchable piezoresistive sensors enabled by multimaterial 3D printing of carbon nanotube/thermoplastic polyurethane nanocomposites," *Polymers*, vol. 11, no. 1, p. 11, Jan. 2019, doi: 10.3390/polym11010011.

[45] J. Tang, Y. Wu, S. Ma, T. Yan, and Z. Pan, "Sensing mechanism of a flexible strain sensor developed directly using electrospun composite nanofiber yarn with ternary carbon nanomaterials," *IScience*, vol. 25, no. 10, Oct. 2022, Art. no. 105162, doi: 10.1016/j.isci.2022.105162.

[46] K. Ogata and Y. Matsumoto, "Estimating movements of human body for the shirt-type wearable device mounted on the strain sensors based on convolutional neural networks," in *Proc. IEEE 41st Annu. Int. Conf. Eng. Med. Biol. Soc.*, 2019, pp. 5871–5876, doi: 10.1109/EMBC.2019.8856722.

Zinan Cen (Member, IEEE) received the B.A.Sc. degree in mechanical engineering from University of Toronto, ON, Canada, in 2021. He is currently working toward the M.A.Sc. degree in mechanical engineering at the TSmart Lab and ASB Lab, University of Toronto, Toronto, ON, Canada.

Fraser Robinson (Member, IEEE) received the B.A.Sc. degree in mechatronics engineering from University of Waterloo, ON, Canada, in 2021. He is currently working toward the M.A.Sc. degree in mechanical engineering at the ASB Lab, University of Toronto, Toronto, ON, Canada.

Authorized licensed use limited to: The University of Toronto. Downloaded on June 08,2024 at 19:06:41 UTC from IEEE Xplore. Restrictions apply.

This article has been accepted for inclusion in a future issue of this journal. Content is final as presented, with the exception of pagination.

Goldie Nejat (Member, IEEE) received the B.A.Sc. and Ph.D. degrees in mechanical engineering from the University of Toronto, Toronto, ON, Canada, in 2001 and 2005, respectively.

She is a Full Professor and Associate Chair for Research with the Department of Mechanical and Industrial Engineering, the University of Toronto. She is the Canada Research Chair with Robots for Society and the Founder and Director of the Autonomous Systems and Biomechatronics Laboratory. She is also an Adjunct Scientist with both KITE, the Toronto Rehabilitation Institute, and the Rotman Research Institute, Baycrest Health Sciences.

Hani E. Naguib received the Ph.D. degree in mechanical engineering from the University of Toronto, Toronto, ON, Canada.

He is currently a Professor with the University of Toronto and the Director of the Toronto Institute for Advanced Manufacturing, Toronto, Canada. His research scope encompasses the area of advanced materials and manufacturing. His major expertise is in the area of smart and active materials; nanostructured polymers and composites; and bio-based materials. His group has applied these materials in a range of industrial and health care technologies, such as sensors, actuators, energy materials, batteries, supercapacitors, smart textiles, and clinical devices. The main goal of his research program is to develop sustainable and transformational materials and manufacturing for energy management and health care.

Authorized licensed use limited to: The University of Toronto. Downloaded on June 08,2024 at 19:06:41 UTC from IEEE Xplore. Restrictions apply.